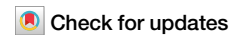


<https://doi.org/10.1038/s42003-024-06939-3>

Transcriptome and acetylome profiling identify crucial steps of neuronal differentiation in Rubinstein-Taybi syndrome



Julien Van Gils¹ ✉, Slim Karkar², Aurélien Barre², Seyta Ley-Ngardigal¹, Sophie Nothof³, Stéphane Claverol⁴, Caroline Tokarski⁴, Jean-Philippe Trani³, Raphael Chevalier³, Natacha Broucqsault³, Claire El Yazidi³, Didier Lacombe¹, Patricia Fergelot¹ & Frédérique Magdinier³

Rubinstein-Taybi syndrome (RTS) is a rare and severe genetic developmental disorder characterized by multiple congenital anomalies and intellectual disability. *CREBBP* and *EP300*, the two genes known to cause RTS encode transcriptional coactivators with a catalytic lysine acetyltransferase (KAT) activity. Loss of CBP or p300 function results in a deficit in protein acetylation, in particular at histones. In RTS, nothing is known on the consequences of the loss of histone acetylation on the transcriptomic profiles during neuronal differentiation. To address this question, we differentiated induced pluripotent stem cells from RTS patients carrying a recurrent *CREBBP* mutation that inactivates the KAT domain into cortical and pyramidal neurons. By comparing their acetylome and their transcriptome at different neuronal differentiation time points, we identified 25 specific acetylated histone residues altered in RTS. We also identified the transition between neural progenitors and immature neurons as a critical step of the differentiation process, with a delayed neuronal maturation in RTS. Overall, this study opens new perspectives in the definition of epigenetic biomarkers for RTS, whose methodology could be extended to other chromatinopathies.

Between 5 and 10% of Mendelian disorders resulting from variants in genes coding for chromatin remodeling factors are directly related to the epigenetic machinery. This group of pathologies associated with genome-wide alterations in the organization of the chromatin fibers are called chromatinopathies. Approximately 75% of them cause neurodevelopmental disorders¹. Among them, Rubinstein-Taybi syndrome (RTS; OMIM #180849, OMIM #613684) is considered as a model of neurodevelopmental disorder linked to epigenetic changes.

This severe congenital syndrome is characterized by intellectual disability together with typical facial and extremity abnormalities associated with other malformations (cerebral, cardiac, renal, or ocular)². Its prevalence in the general population is estimated between 1/100,000 and 1/125,000 births³. More than 600 cases have been reported in the literature⁴.

Two paralogous genes are associated with the determinism of RTS: *CREBBP* (CREB-binding protein; KAT3A; NM_600140) in about 60%

of cases (RTS type 1) and *EP300* (E1A-binding protein p300; KAT3B; NM_602700) in about 8% (RTS type 2)^{5,6}. They each comprise 31 exons^{7,8} and code respectively for the CBP and p300 proteins, the only two members of the Lysine Acetyl transferase 3 family (KAT3). These proteins are highly conserved transcriptional co-activators that possess a lysine acetyltransferase (KAT) catalytic domain responsible for the acetylation of histone lysine residues but also of other proteins⁹. CBP and p300 promote transcription by creating a chromatin environment favorable to gene expression in different ways. They act as scaffolding proteins by recruiting various transcription initiation factors, notably the TATA-binding protein and TFIIB^{10,11}. Both proteins orchestrate the regulation of the transcription machinery from the basal promoter to the enhancers of the target genes. In drosophila cells, CBP directly stimulates both RNA Polymerase II recruitment and the ability to traverse the first nucleosome highlighting a role in elongation, a second step of transcription regulation at promoters¹². They also act as bridges linking

¹Department of Medical Genetics, University Hospital of Bordeaux and INSERM U1211, University of Bordeaux, Bordeaux, France. ²Bordeaux Bioinformatic Center CBIb, University of Bordeaux, Bordeaux, France. ³Aix Marseille Univ, INSERM, Marseille Medical Genetics, Marseille, France. ⁴Bordeaux Proteomic Platform, University of Bordeaux, Bordeaux, France. ✉e-mail: julien.van-gils@chu-bordeaux.fr

transcription factors binding DNA or *cis*-regulatory elements to the transcription machinery. They also catalyze acetylation of histone and non-histone proteins as well as of the acetyltransferase domain of p300/CBP through their KAT activity¹³.

CBP and p300 play a crucial role during development by controlling the proliferation and differentiation of different cell types, particularly in the nervous system¹⁴. In mammals, both proteins are required for neural tube closure at the embryonic stage¹⁵. Moreover, the loss of function of one of the two proteins in heterozygous *Cbp*^{+/-} or *p300*^{+/-} mice is compensated by overexpression of the other in later stages of development¹⁶. This indicates that these two proteins play redundant roles during early development but that a global level of acetylase activity catalyzed by both CBP and p300 is essential for a proper embryonic development. In normal mice, several nucleosomal positions are acetylated during learning tasks. These marks are associated with specific stages of memory development. For example, histone H3 acetylation increases rapidly in the hippocampus and lateral amygdala after contextual fear conditioning¹⁷, whereas spatial memory acquisition is associated with H2B and H4 acetylation in the hippocampus¹⁸. Other studies in mouse models have shown that histone acetylation changes may be restricted to the promoters of memory-associated genes, such as the *BDNF* Neurotrophin gene (involved in synaptic plasticity and long-term memory maintenance). For example, at the *BDNF* promoter, hyperacetylation of histones H3 is necessary for memory reconsolidation of conditioned fear memory¹⁹ whereas the extinction of this conditioned fear memory is associated with hyperacetylation of H4 in neurons of the prefrontal cortex²⁰. These data thus indicate that histone acetylation is involved in memory and plays a key role in neuronal plasticity¹⁷. Modulations of histone acetylation have been demonstrated not only in mouse RTS models but also in lymphoblastoid cell lines from RTS patients^{21,22}.

In humans, the molecular pathways impacted by these alterations during neurodevelopment are unknown, especially in pyramidal neurons which are the precursors of hippocampal neurons responsible for memory encoding and storage²³. To date, one of the main clinical challenges is to improve the intellectual and memory deficiency for RTS patients which requires a better understanding of the mechanisms governing long-term memory, strongly impaired in this syndrome. A cellular model closer to human pyramidal neurons is therefore essential for our understanding of memory dysfunction in RTS. Recently, a first model of neurons derived from induced pluripotent stem cells (iPSCs) reprogrammed from blood cells of type 1 and type 2 RTS patients was used to investigate transcriptomic changes that may be involved in these mechanisms^{24,25}. However, the consequences of *CREBBP* or *EP300* variants on histone acetylation on neuronal differentiation has not been addressed.

To this aim, we investigated the correlation between changes in gene expression and histone acetylation profile in hiPSC-derived neurons for RTS patients and controls. Our results highlighted the critical precocious transition phase in the development of the neuron in RTS patients by identifying the histone marks and the biological pathways impacted.

Results

Neurons derived from RTS patient's cells display a delayed differentiation

In order to investigate neuronal differentiation in patients affected with RTS, we derived induced pluripotent stem cells (hiPSCs) for 4 RTS patients (RTS1, RTS2, RTS3 and RTS4) carrying the same *CREBBP* missense mutation (c.3832 C > T/p.Glu1278Lys) that specifically abolishes CBP KAT activity²⁶ (Table S1). HiPSCs from two healthy controls were used as reference (C1 and C2). HiPSC-derived neuronal progenitors were produced in 10 days²⁷. Neural expansion occurred during the following 10 days until the typical appearance of neural rosettes at D20. The transition from neural progenitors to immature neurons began at D20 with the constitution of a neuronal network starting from the rosettes up to D30–40. The differentiation was maintained until D60 for production of mature cortical and pyramidal neurons forming a clearly visible neural network (Figs. 1a, S2, S3). All subsequent analyses were performed at D10, D20, and D60.

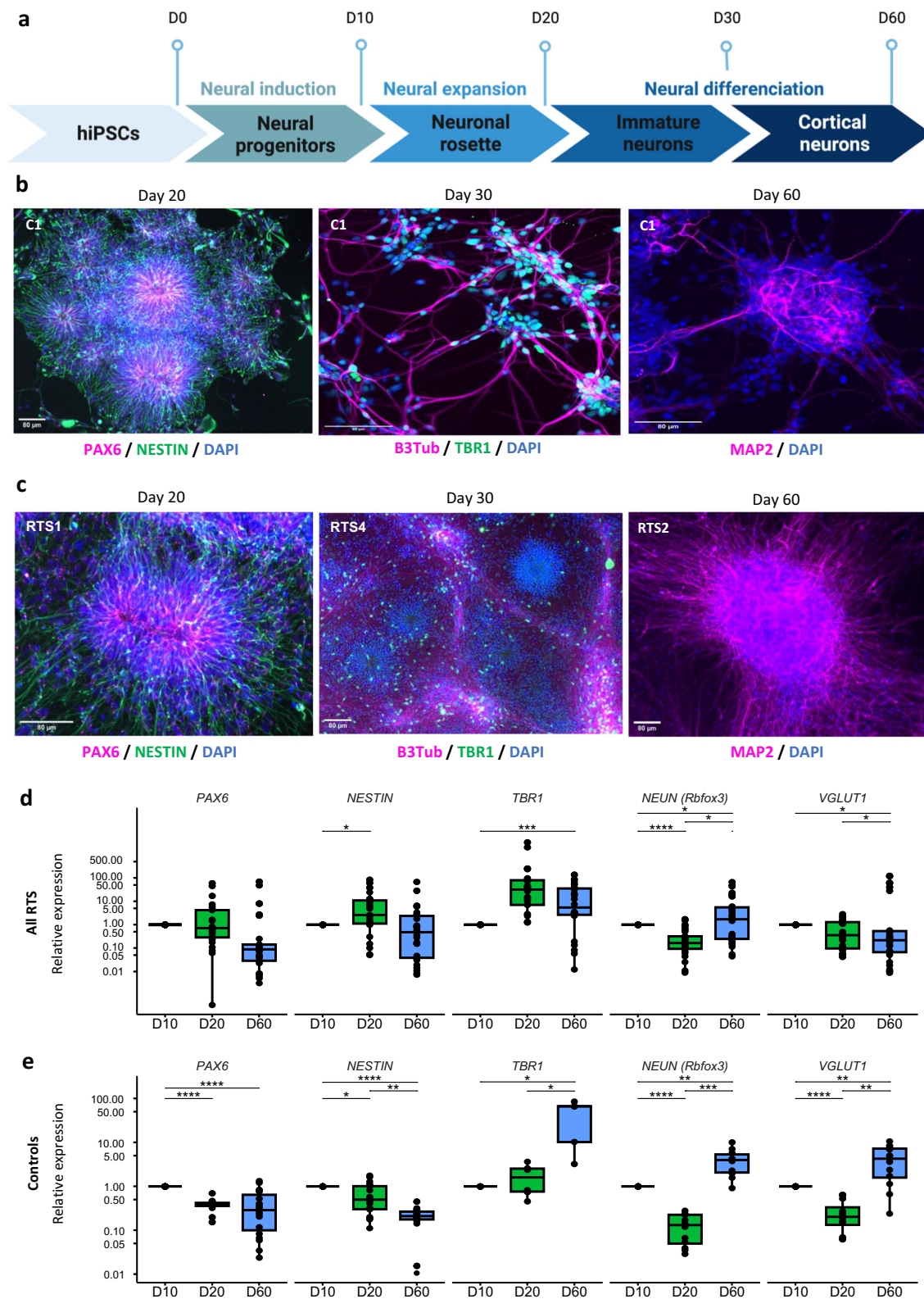
In order to characterize each differentiation step, we first determined the percentage of cells expressing stage-specific markers by immunofluorescence staining (IF) and flow cytometry. Between 95.1% and 98.7% of control cells are positive for at least one neural progenitor marker at D10 (PAX6 and/or NESTIN) compared to 89.7–96.7% of positivity in RTS cells (Fig. S1a). At the rosette stage (D20), the majority of cells (controls and RTS) showed a positive IF staining for the neuroectodermal stem cell markers, NESTIN and PAX6 (Figs. 1b, c and S2). The transition from the neural progenitor to immature neurons was confirmed between D20 and D30 by a positive B3 Tubulin (pan-neuronal marker) and TBR1 (Immature neurons) staining both in control and selected RTS cells. We observed a decrease in the percentage of neuronal progenitors at D30, where 49.7% (C1) and 50.3% (C2) control cells are PAX6/NESTIN double negative cells versus 38.7% (RTS1) to 76.3% (RTS2) of RTS cells. At D30, the loss of pluripotency and the transition to immature neurons follows the same kinetics for controls and patients with 93–96.8% of control cells and 88.7–96.4% of RTS cells negative for the pluripotency marker SOX2. At D30, 25.8–53.5% of control cells are positive for B3 Tubulin versus 49.3–58.4% for RTS cells (Fig. S1b). At D60 we confirmed the differentiation into mature cortical neurons positive for MAP2 and the formation of a rich neuronal network in both controls and patient's cells (Figs. 1b, c and S3). By quantifying immunostaining, we found no significant difference between RTS patients and controls, either for PAX6 and NESTIN at D20 or for MAP2 in mature neurons at D60 (Fig. S4). We also studied the morphology of NESTIN and MAP2 networks by analyzing interconnection of the neuronal network branches (Fig. S5). With regard to the early time point (NESTIN at D20), we observed no significant difference of network branches interconnection between RTS patients and controls. In contrast, for MAP2 labeling of mature neurons (D60), we observed significant differences with a network showing fewer interconnections between branches in RTS patients compared to controls. The morphology of neural marker networks therefore appears to be affected in RTS patients during neuronal maturation.

We then compared the kinetics of neuronal differentiation at D20 and D60, in controls and patients by RT-qPCR using D10 as a reference. The expression of the neural progenitor markers (*PAX6* and *NESTIN*) follows a similar trend for controls and patient cells. Between D20 and D60, we observed a significant increase in the expression of markers of transition from immature (*TBR1*) to mature (*NeuN*) neurons and expression of markers of glutamatergic (*VGlut1*) neurons in control cells. In contrast, in patient cells, we observed a clear increase for TBR1 at D20 and a decreasing trend at D60. At D60, *NeuN* is slightly increased while *VGLUT1* expression is significantly decreased (Fig. 1d, e). We concluded on a similar dynamic in the initiation of differentiation between controls and RTS patients but a delay in the transition between neuronal progenitor and immature neurons at D20 in RTS patients with a repercussion on the expression of mature neurons markers at D60.

Confidence map of altered histone acetylation in RTS patients during neuronal differentiation

All four core histones are acetylated by CBP/p300²². However, an exhaustive map of the impact of *CREBBP* variants on the histone acetylation profile has never been reported to date in RTS. To fill this gap, we performed an acetylome analysis by LC-MS/MS during neuronal differentiation at D10–D20–D60 in control and RTS cells. For each condition, two biological replicates corresponding to two independent differentiation experiments were used (Fig. 2a).

We focused our attention on the quantification of acetylated residues for the four core histones, H2A, H2B, H3, and H4. At each of the 3 neuronal differentiation time points (D10, D20, and D60), we identified a total of 35 acetylation sites, 3 for H2A (K5, K9, and K95), 14 for H2B (K5, K11, K12, K15, K16, K20, K23, K34, K43, K46, K85, K108, K116, and K120), 10 for H3 (K9, K14, K18, K23, K27, K36, K37, K56, K79, and K122) and 8 for H4 (K5, K8, K12, K16, K31, K77, K79, and K91) (Table S4). Principal component analysis (PCA) showed a distinctive separation between the neuronal progenitor stage (D10) and the mature neuron stage (D60) with a subclustering of



control and patient's cells at both time points. There was no obvious difference at the progenitor/immature neuron transition stage (D20) for controls and RTS cells. The hiPSCs-derived neurons from the RTS patients are well separated from the controls at each of the 3 differentiation stages (Fig. S6a).

As the dynamic of histone acetylation during neuronal differentiation is not known in RTS, we explored the kinetics of acetylation of each

individual amino acid residue individually in controls (Fig. 2b) and RTS patients (Fig. 2c). An acetylation site is as considered hypoacetylated for a $\log_2\text{ratio} \leq 1$ and hyperacetylated for a $\log_2\text{ratio} \geq 1$. We choose the progenitor stage (D10) as the reference. In control samples, we did not observe any significant changes in the kinetics of acetylation for H4 lysines throughout the differentiation process. In contrast, H2A acetylation level

Fig. 1 | Morphological and molecular characterization of hiPSC-derived neurons during neuronal differentiation of controls and Rubinstein–Taybi syndrome (RTS) hiPSC. **a** Timeline of the main steps of neuronal differentiation from hiPSCs to mature cortical neurons. The protocol was adapted from Shi et al.²⁴. **b, c** Immunofluorescence characterization during neuronal differentiation for controls (**b**) and RTS patients (**c**). Positive staining of neuronal progenitor at D20 for the NESTIN and PAX6 markers. Transition to immature neurons occurs between D20 and D30 as evidenced by positive staining for B3Tub (pan-neuronal marker) and TBR1 (Immature neurons). The neural network gradually develops from the periphery of neural rosettes. The mature neuronal network is evidenced at D60 by a positive staining to MAP2 (mature cortical neurons). Nuclei are counterstained with DAPI. **d, e** Molecular characterization of controls (**d**) and RTS patients (**e**) during neuronal differentiation. Gene expression level was determined by RT-qPCR at 3

different time points (D10–D20–D60). D10 was used as the reference as most genes are not expressed in hiPSCs. Expression was normalized to two housekeeping genes (HPRT and PPIA). The box plots (green for D20 and blue for D60 display the median relative expression level. The lower (Q1) and upper (Q3) quartile represent data outside the 9–91 percentile range. Data falling outside the Q1–Q3 range are plotted as outliers. All data points for control samples are presented as the result of two biological replicates followed by two technical replicates. All data points for RTS samples are presented as the result of four biological replicates followed by two technical replicates. Statistical significance was determined using an *F*-test on two-way ANOVA for paired sample analysis and *p*-values were corrected for multiple comparison using Benjamini–Hochberg control of the false discovery rate, with * *p* value < 0.05, ** *p* value < 0.005, *** *p* value < 0.0005, and **** *p* value < 0.00005.

slowly decreases for K5, K9, and K35 from D10 to D60. At D60, hypoacetylation mainly concerned H2B and H3 with changes for five (H2BK5, H2BK12, H2BK43, H2BK46, H2BK108) and four (H3K18, H3K37, H3K56, H3K79) amino acid residues, respectively (Fig. 2b). Among these marks, two were hyperacetylated, H2BK120 transiently at D20 whereas H3K36 hyperacetylation was maintained up to D60 (Fig. 2c). In RTS cells, most of the changes occurred at D20. Compared to control, we observed a different kinetic profile with three sites transiently hypoacetylated: H2BK43, H4K77, and H4K91 and two sites transiently hyperacetylated (H2AK5 and H2AK9). For H2B and H3, the level of acetylation decreases for ten sites between D20 and D60 (H2BK5, H2BK12, H2BK43, H2BK46, H2BK108, H2BK120; H3K18, K3K36, H3K37, H3K56) (Fig. 2c). At D60, the majority of these sites show an inverse trend of acetylation between controls (hypoacetylation) and RTS patients (hyperacetylation). We also observed a marked increase in acetylation for histone H4, in particular for H4K31 in RTS patients at D60 compared to controls.

Overall, the analysis of the dynamics of histone acetylation during neuronal differentiation in RTS indicates that both hypo- and hyperacetylation occurs in the presence of a *CREBBP* variant. Furthermore, changes in acetylation are most pronounced for H2B and H3 sites with modulations occurring earlier in RTS cells, at the progenitor/immature neuron transition stage.

Confidence map of altered histone acetylation in RTS patients during neuronal differentiation

To explore specific changes in acetylated CBP sites in RTS patients during neuronal differentiation, we performed differential analysis between RTS patients and controls at the three selected time points. We quantified the acetylation level for each lysine residue and each histone during neuronal differentiation. To summarize acetylation data, we calculated the log₂ acetylation ratio based on the median of conserved sites for different isoforms of each protein in RTS patients compared to controls. We obtained a confidence map of CBP-dependent histone acetylation sites in RTS cells during neuronal differentiation. Results are presented separately for each RTS patient (Fig. 2d–g). Indeed, due to the inter individual differences, averaging the data for all patients versus controls led to identify 15–21% of histone marks shared between time points while combining the results of each RTS patient revealed differences for 73–79% of the analyzed sites (Fig. S6b). In comparison to controls, we considered that altered hypoacetylated histone residues in RTS as sites showing a log₂acRatio ≤ −1 difference in at least 3 out of the 4 RTS patients in at least 1 out of the 3 time points. Based on these criteria, among the 35 identified acetylation sites, we selected 25 candidate histone acetylation sites (three in H2A, ten in H2B, eight in H3 and four in H4) (Fig. 2d–g and Table S4). Our differential analysis showed that hypoacetylation is more pronounced for H2B and H3 sites, in particular for H3K23 and the well-known CBP-dependent H3K27 residue (Fig. 2e, f). N-terminal H4 Lysine residues (H4K8, H4K12, and H4K16) are also hypoacetylated as reported in other models^{22,28} (Fig. 2g). The level of acetylation of many C-terminal H2B and H3 sites was reduced in RTS patients compared to controls indicating that CBP also contributes to the post-translational modification of core histone globular domains. Regarding the

differential kinetics of acetylation during neuronal differentiation, hypoacetylation of the 25 sites is detectable as early as the neuronal progenitor stage in RTS and persists until the mature neuron stage except for H2AK5 and H2AK9, transiently hypoacetylated at D10 only (Fig. 2d).

Altogether, this quantitative analysis indicates that the acetylation of the four core histones is altered at different levels in CBP-deficient cells. Acetylation level of H2B, H3K23, H3K27, and of H4 N-terminus are particularly impacted during in vitro neuronal differentiation while acetylation of the N-terminus of H2A (H2AK5 and H2AK9) is impacted by *CREBBP* variants only at the very early phase of the differentiation process (neuronal progenitor).

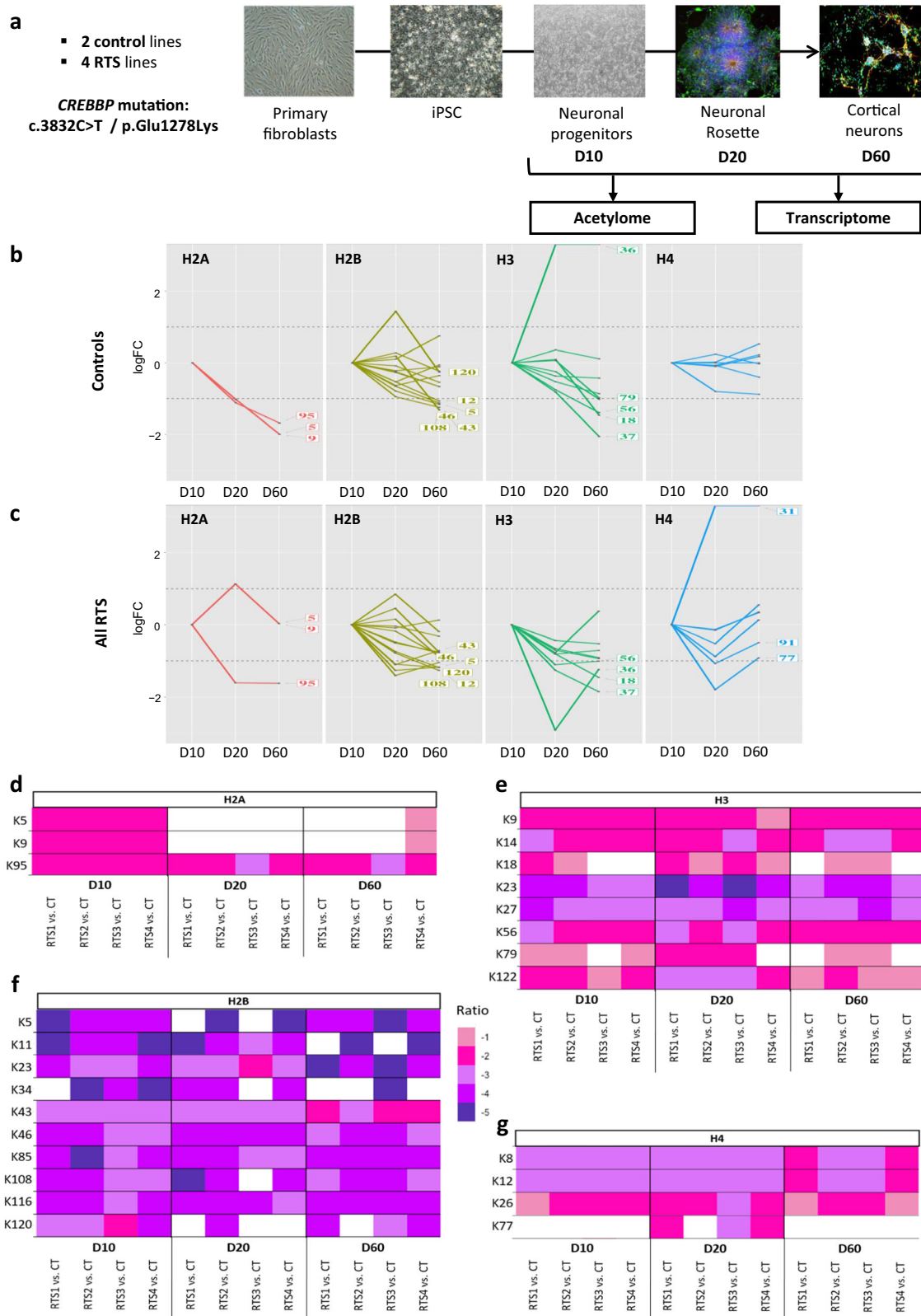
Transcriptomic analysis reveals key stage in neuronal development in RTS

In order to identify biological processes (BPs) altered in RTS during neuronal development, we performed a transcriptomic analysis of hiPSC-derived neurons for the two controls and the four RTS patients at the three neuronal differentiation stages (Fig. 2a). Consistent with the different populations of cells at the different steps of differentiation, the PCA showed a clear clustering of samples at the three time points. Compared to controls, we did not distinguish any significant variability between controls and RTS patients at D10 and D60. However, we observed a distinct separation of controls and RTS cells at D20 (Fig. 3a). These results were confirmed using an unsupervised heatmap that distinguishes 3 main clusters. Controls segregated within the same cluster regardless of the differentiation stage. RTS cells formed two distinct clusters: one grouping the samples at D10 and D60 and the second one corresponding to the RTS cells at D20 (Fig. 3b).

Differential expression analysis between RTS and control hiPSC-derived neurons revealed a total of 2973 differentially expressed genes (DEGs) including 374 DEGs at D10, 2454 at D20, and 416 at D60. DEGs were mostly downregulated at D10 (55%) and D60 (61%), in contrast to D20 where 58% of DEGs were upregulated ($|\log_2\text{Foldchange}| \geq 1$; FDR < 0.05). Remarkably DEGs at D20 represent 82.5% of the total DEGs, of which 2232 (75% of total DEGs) are exclusively deregulated at this progenitor/immature neuron transition stage (Fig. 3c, d). Hence, the major and transient increase in DEGs at D20 could reflect a decisive transition stage in priming the alterations of neuronal identity in the disease (Fig. 3e). Consistent with the acetylome profiling, these results pinpoint D20 as a key stage to decipher the mechanisms underlying defects in neuronal differentiation of RTS hiPSC-derived neurons.

Analysis of BP related to neurodevelopment suggest an altered neuronal identity in RTS

Using Gene Ontology (GO), we then looked at BPs associated with DEGs in the different conditions and samples. We identified 55 GO terms enriched at D10 (32 downregulated genes (DRG) and 7 upregulated genes (URG)-enriched GO terms), 771 at D20 (72 DRG and 765 URG-enriched GO terms) and 196 at D60 (92 DRG and 118 URG-enriched GO terms). Due to the large number of DEGs-associated BPs, we first looked at GO terms retrieved for the top 15 most significantly DRG and URG (Fig. S7). From D10, 3/7 of URG-enriched GO terms were associated with



neurodevelopment (“spinal cord association neuron differentiation”, “neurogenesis” and “nervous system development”). At D20, this increase in significant GO terms enrichment correlates with the number of DEGs identified at this stage. The most significantly deregulated BPs concerned more general mechanisms such as “cell differentiation” or “tissue development” (Fig. S7b). However, top DRG-enriched GO terms revealed

many BPs involved in neurodevelopment (5/15), such as “central nervous system development”, “generation of neurons”, “neuronal differentiation”, “neurogenesis” and “nervous system development”, mirroring what is observed at D10. At D60, “nervous system development” is again significantly enriched in URG. Interestingly, we also identified BPs associated with skeletal development: “positive regulation of osteoblast

Fig. 2 | Acetylome profiling during neuronal differentiation of controls and RTS patients hiPSCs. **a** Schematic overview of the samples used and steps of analysis. hiPSCs were derived from primary fibroblasts from two healthy donors (controls) and four patients affected with RTS carrying the same *CREBBP* mutation: c.3832 C > T/p.Glu1278Lys. All hiPSCs clones were differentiated into cortical and pyramidal neurons. Acetylome analysis by mass spectrometry (LC-MS/MS) focused on core histones proteins (H2A, H2B, H3, and H4) and gene expression analysis by high-throughput RNA-sequencing was performed at three time points during the differentiation process (D10, D20, and D60). For each condition, two biological replicates corresponding to two independent differentiation experiments were used. **b, c** Kinetics of histone acetylation for H2A, H2B, H3, and H4 during neuronal differentiation at D10, D20, and D60 in controls (**b**) and RTS patients (**c**). The log₂ ratio for each acetylation site of the indicated histones is shown for each time point.

differentiation” as URG-enriched GO term and “skeletal system development” as DRG-enriched GO term (Fig. S7a), an interesting observation in light of RTS patient’s phenotype.

In order to identify genes of interest and a candidate biological pathway associated with the delayed involved neuronal differentiation process observed in RTS patients, we searched for DEGs significantly enriched in BPs found in at least three out of the six conditions (URG and DRG enriched GO terms for D10, D20, and D60). This enabled us to identify 50 DEGs-enriched BPs significantly deregulated in at least at two out of three different time points during differentiation (Fig. 4a and Table S5). Among them, many GO terms are linked to developmental processes (such as “regulation of system process” or “embryonic morphogenesis”) and to RNA synthesis, such as “positive regulation of RNA metabolic” and “biosynthetic processes”, “position regulation of transcription DNA-templated”.

Six (12%) of the identified DEGs-enriched BPs are associated to neurodevelopment. The hierarchical organization of these BPs revealed two distinct branches (Fig. 4a). We analyzed the expression of DEGs associated with BPs at each end of the phylum (the most specific): “Brain development” and “Neuron differentiation”. At D10, the DEGs associated with these two BPs were not significantly deregulated in RTS patients compared with controls. However, they were both significantly associated with up or down regulated DEGs at D20 and downregulated at D60 (Fig. 4a).

Consistent with this trend, we then looked at the list of DEGs that were specifically up- or down-regulated at D20 and down-regulated at D60. We identified 5 DEGs associated with “Brain development” and 5 DEGs associated with “Neuron differentiation” (Fig. 4b, c). Due to an overlap of DEGs within these two BPs, this resulted in a list of 7 candidate DEGs detailed (Fig. 4d). *ZIC3*, *LMX1A* and *SOX3* are shared by the two above-mentioned BPs (Table S6). Expression of *NEUROG2* and *SOX3* is decreased at D20 then increased at D60 in RTS cells compared to controls. *ZIC3* expression is decreased at D10 and then increased at the end of differentiation. *FGF10* is not significantly deregulated at D10 but follows the same kinetics of increase thereafter. *RSPO2*, *LMX1A* and *CA10* are upregulated in RTS cells throughout the whole neuronal differentiation process.

The analysis of protein–protein interaction network for these DEGs, enabled us to identify functional interactions between five of these seven DEGs (*NEUROG2*, *SOX3*, *ZIC3*, *RSPO2*, and *LMX1A*), all involved in the WNT/b-catenin pathway. This further suggest a direct implication of this pathway in the delayed neuronal differentiation in RTS cells (Fig. 4e).

Multi-OMICS data integration associate specific histones marks and DEGs with the key stages of neuronal differentiation in RTS

In order to integrate our transcriptome and acetylome data, we used the multi factorial analysis (MFA) framework²⁹ to produce a joint analysis of Histone acetylation and gene expression. In a first MFA (Fig. 5a, c), we used the 25 selected histone marks as the first group of variables (Fig. 2 and Table S4) and the top 20 DEG from each time point (46 unique genes) as the second group of variables (Table S7). For the second MFA (Fig. 5b, d), we selected the same 25 histone acetylation marks as the first group of variables and the 7 DEGs associated to neurodevelopment in the second group (Fig. 4d).

An acetylation site is considered hypoacetylated with a log₂ratio ≤ 1 and hyperacetylated with a log₂ratio ≥ 1 and the position is labeled on each graph. D10 was chosen as the reference value for the analysis. **d–g** Mapping of differential analysis of acetylome of CBP-dependent histone marks during neuronal differentiation in RTS patients compared to controls. Heatmaps of the acetylome during neuronal differentiation. The heatmaps display the log₂ ratios for acetylation sites on the protein core histones H2A (**d**), H2B (**e**), H3 (**f**), and H4 (**g**) for each RTS patient (RTS1–RTS4) compared to controls at the 3 time points of the neuronal differentiation (D10, D20 and D60). An acetylation site is considered hypoacetylated with a log₂ratio ≤ 1 and is displayed as a magenta gradient. Values with a log₂ratio between −1 and 1 are shown in white. We considered a candidate histone mark altered in RTS as mark that is hypoacetylated in at least 3 out of the 4 RTS patients analyzed and for at least 1 out of the 3 time points.

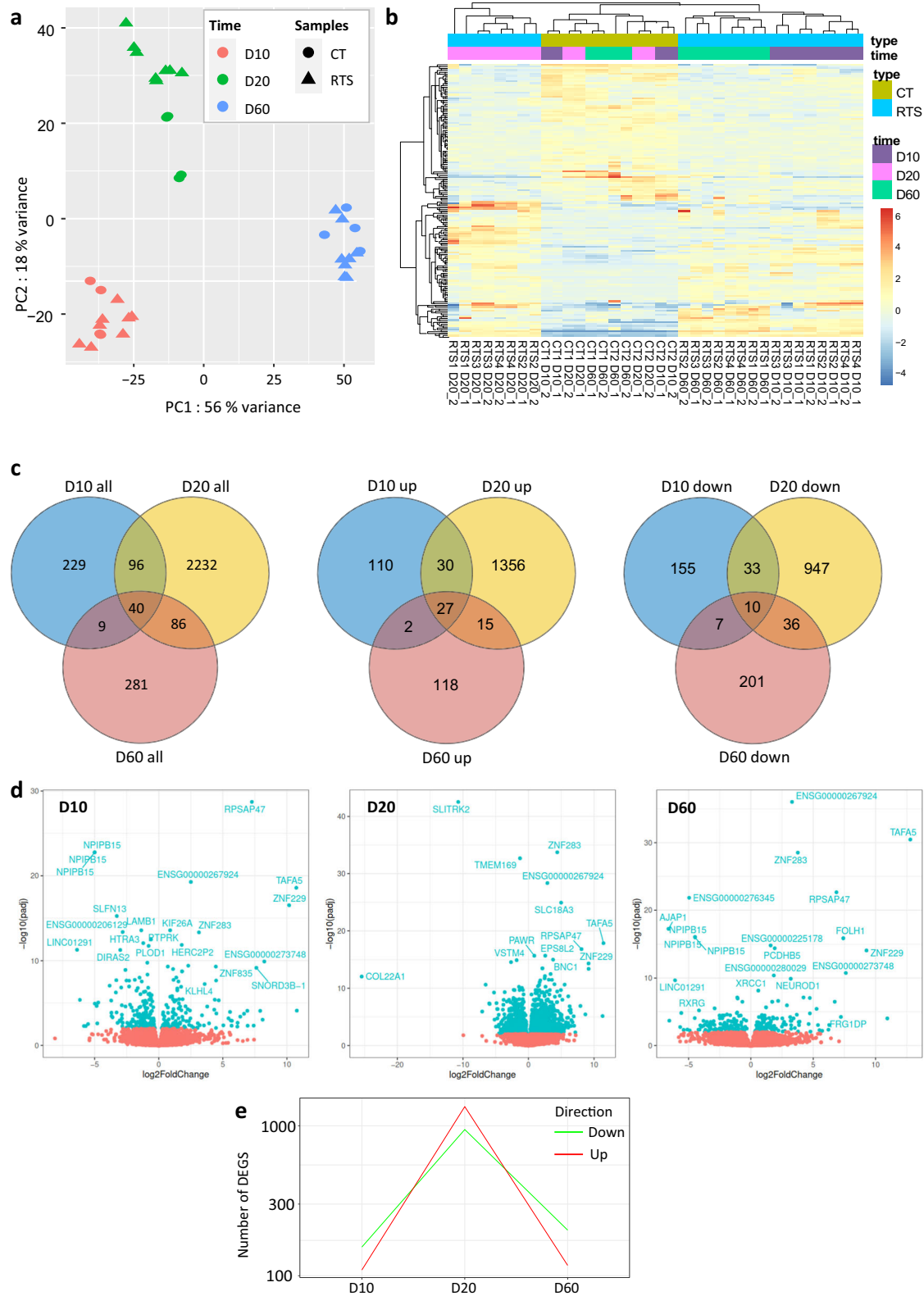
By combining the two-omics modalities in a single multivariate analysis, we observed a clear separation of signals for samples at D20 samples compared to D10 and D60 as described above (Fig. 3a, b). By comparing the 25 histone marks and the 46 DEGs, we observed that this separation depends on 12 histone marks and 21 genes (Fig. 5a), associated with the first component in the bootstrap analysis (Fig. 5c). Moreover, the first component mostly separates samples for D20 from samples from D10–D60 samples when restricting the analysis to the 7 neurodevelopmental genes (Fig. 5b). The bootstrap analysis revealed that the expression levels of two genes (*SOX3* and *NEUROG2*) can be safely associated with the acetylation profile of 11 Lysine residues (H2AK95, H2BK5, H2BK43, H2BK46, H2BK108, H3K18, H3K23, H3K56, H3K79, H3K122, and H4K77) (Fig. 5d) again highlighting H2B and H3 as major targets of CBP in the control of gene expression during neuronal differentiation.

Discussion

One of the priorities in neurodevelopmental disorders and in particular Rubinstein–Taybi syndrome is to identify the mechanisms leading to intellectual disability. This crucial milestone involves the identification of biological pathways disturbed in the disease but also the identification of biomarkers for diagnostic and therapeutic purposes. In RTS, a loss of function of its KAT activity impairs the main function of CBP in transcriptional regulation. Among KAT substrates, acetylated histones are essential actors in the regulation of gene expression at the chromatin level, making the syndrome a model of congenital disorder associated with alterations of the epigenome. In order to uncover the role of CBP KAT domain in the neurological manifestation of the disease, we investigated four patients with the same *CREBBP* missense mutation (c.3832 C > T/p.Glu1278Lys) that abolishes the KAT domain of CBP²⁶.

Over the recent years, the contribution of iPSC-derived cell models for neuronal differentiation emerged as an essential tool for questioning and understanding the regulation of epigenetic mechanisms during neurodevelopment^{30–35}. Taking advantage of hiPSC-derived neurons, we jointly mapped the transcriptome of neuronal progenitors, immature neurons and cortical neurons together with the dynamic of the histone acetylome in RTS and control cells. Our results provide a detailed repertoire of Lysine residues for which acetylation changes are dependent on CBP. We further identified the transition between neuronal progenitor and immature neurons as the key step of transcriptomic deregulation during neurodevelopment in RTS.

A first model of iPSC-derived neurons for four *CREBBP* and two *EP300*-mutated RTS patients revealed an altered morphology of neurons with a reduced average branch length and increased branch number. In this model, RTS neurons were able to generate action potentials but are hypoexcitable²⁴, in particular for cells carrying a missense variant. Interestingly, this hypoexcitability causes impairment at a later stage of differentiation. This observation is consistent with our morphological analysis and RT-qPCR results, which show a delayed maturation in RTS patient’s cells that do not reach the glutamatergic neuron stage in our model. Moreover, we observed an altered neuronal network at the last stage of neuronal differentiation.



The impact of CBP and p300 on the proliferation and differentiation of different cell types and in particular the nervous system was well demonstrated in animal models¹⁴. In the mouse, the loss of CBP/p300 induces a downregulation of neuronal genes associated with a decrease of pro-neural transcription factor binding at the promoters and enhancers of canonical neuronal genes and hypoacetylation of H3K27³⁶. A large mapping of CBP-p300-regulated acetylation sites identified thousands of acetylation sites and

in particular at the 4 core histones. Acetylation of H2B and H3 are the most dependent on CBP and p300²². In human pathology, the impact of CBP/p300-related histone acetylation deficits is much less known. In RTS patients lymphoblastoid cells, acetylation profiling of the four nucleosomal histones showed a general reduction of bulk acetylation levels compared to controls, particularly for histone H2B and H2A but without specifying the amino acid residues impacted²¹.

Fig. 3 | The neural progenitor/immature neuron transition appears as a key stage of neuronal development in RTS. **a** PCA of gene expression data for the 1000 most variable genes for all patients and controls. The two major components are shown (PC1, x-axis; PC2, y-axis). **b** Heatmap of control- and RTS-derived neurons at D10 (red), D20 (green), and D60 (blue), showing that RTS patients cluster separately from controls at D20, suggesting a different expression profile at this transition time point between neural progenitors and immature neurons. Only genes with $\text{padj} < 0.01$ and $|\log_2\text{FC}| \geq 1$ are shown. **c** Venn diagram comparing the DEGs found at the three differentiation time points in RTS versus control cells. The comparison is performed for all (left), upregulated (middle) and downregulated (right) DEGs.

Our kinetic acetylome analysis provided a map of the specific acetylation sites altered in KAT-mutated cells. We identified 25 hypoacetylated lysine residues in neurons derived from RTS patients with variations depending on the differentiation stage. The differences in abundance between the different marks could be likely explained by the activity of other KATs, including p300 or the involvement of histone deacetylases (KDACs). Overall, we found that the *CREBBP* variant target all four core histones but H2B and H3 are the most impacted throughout differentiation. We confirmed here in humans some of the results obtained in the mouse models, notably the major hypoacetylation of H2BK5, H2BK11, H3K23, and H3K27. In addition, acetylation of several residues deposited by other enzymatic complexes were also impacted such as H3K9 catalyzed by KAT2A/B, H3K23 catalyzed KAT6A/B, or H4K16 deposited by KAT8^{37–39}. Acetylation of H2BK15, K16, and K20 do not seem CBP-dependent. Recently, the H2B N-terminal acetylation (H2BNTac) was proposed as a useful marker for predicting CBP/p300 target genes and a good predictor of enhancer strength⁴⁰. However, multiple H2BNTac sites are found at the same genomic regions, with 92–99% of H2BK5ac and H2BK11-K12ac site peaks overlapping with H2BK16ac and H2BK20ac which could explain that K15, K16, and K20 residues were not identified in our study.

Furthermore, we confirmed alteration in the level of acetylation of many previously reported C-terminal sites corresponding to the globular domain of histones (H3K56, H3K122, and H2BK120)^{22,41–43} and identified novel targets mainly on H2B but also H2AK95 and H3K79. Finally, hypoacetylation was maintained for the vast majority of histone marks identified across neuronal differentiation except for the N-terminal sites of H2A: H2AK5 and H2BK9 impacted only at the early neuronal progenitor stage.

In parallel to the profiling of histone acetylation, we aimed at identifying the biological processes altered during neuronal differentiation in RTS by performing a transcriptional analysis at the three main neuronal differentiation timepoints. This enabled us to identify the neuronal progenitor to immature neurons transition stage as particularly impacted in RTS cells. This was accompanied by a marked increase in the number of DEGs with 82.5% of total DEGS identified at this stage (with 75% of total DEGS identified exclusively at this stage) with a majority of over-expressed genes.

A previous transcriptomic analysis of hiPSC-derived neurons from RTS patients did not reveal any significant DEGs. This divergence might depend on the variability of the patients' genetic background and cognitive deficits, as well as on the efficiency of hiPSC neuronal differentiation and neuronal functional maturation²⁵. To overcome this variability, our strategy was to include only patients with the same *CREBBP* pathogenic variant even though patients had different cognitive profiles (Table S1). The discrepancies between the two studies may also lie on the methodological choice, as the transcriptome in the above-mentioned study was carried out at D35 and D70 of differentiation, i.e., after the critical transition stage that we identified here. According to our protocol, D35 corresponds to a stage of neuronal maturation of the immature/mature neuron transition²⁷.

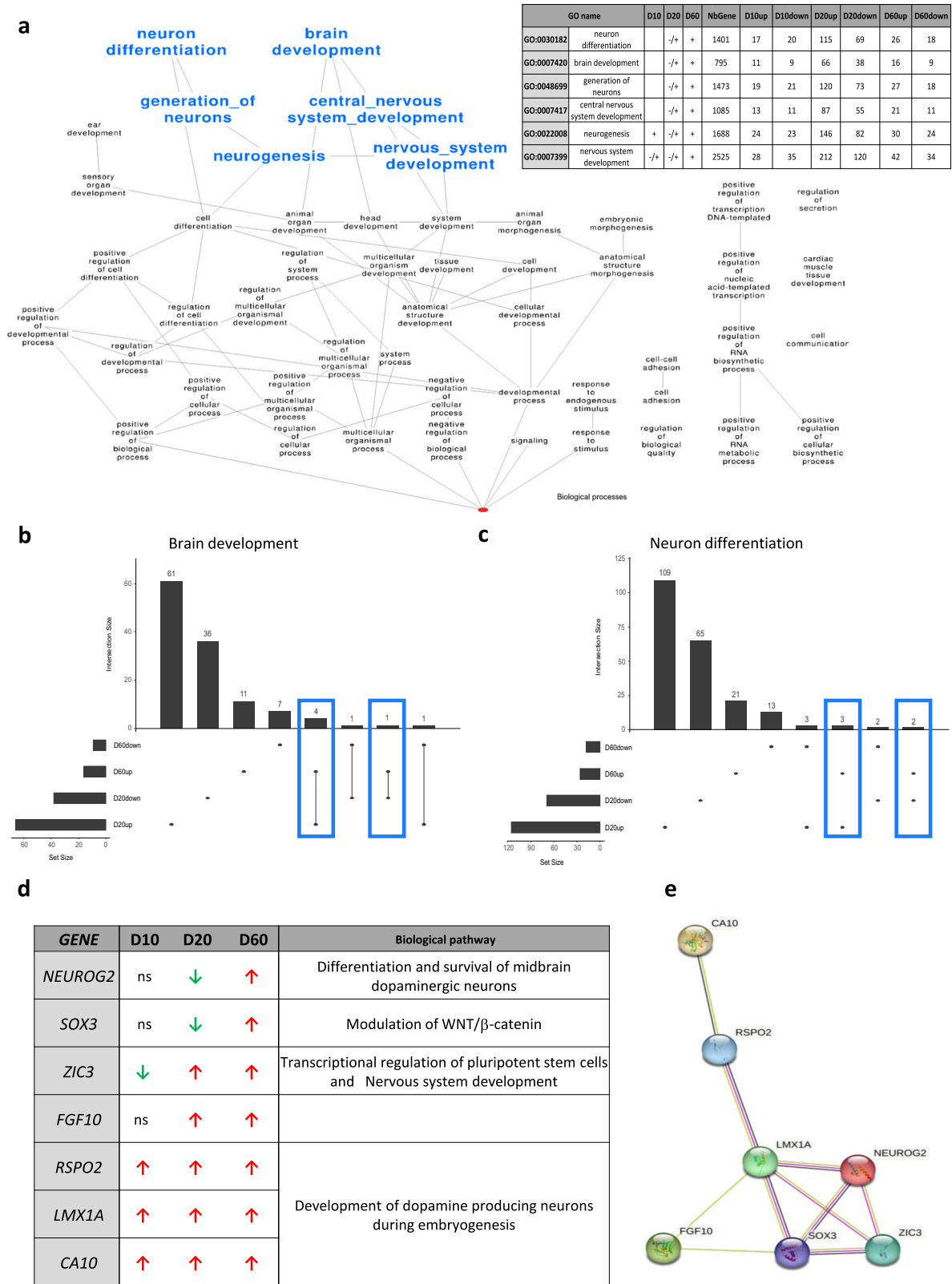
Twelve % of identified BPs are linked to neurodevelopment, and in particular to neuronal differentiation and brain development. All these BPs are associated with DEGS found at D20 and significantly associated with down regulated genes at the end of neuronal maturation. Moreover, by looking at the evolution of the kinetics for the most significant DEGS-enriched GO terms, we noticed a switch in expression for early stages, since at D10, BPs associated with overexpressed genes (URG) are predominantly

involved in neurodevelopment, whereas at D20, genes associated with neurodevelopment correspond to downregulated DEGs (Fig. S7). Based on the DEGs identified and RT-qPCR characterization data, we hypothesized a strong transcriptional deregulation at an early stage of development in RTS patients that might impact neurodevelopmental pathways by altering neuronal maturation. This delayed maturation may explain the shift in expression of neuronal differentiation genes at a late stage of development. Earlier work supported this hypothesis by demonstrating an aberrant upregulation of genes involved in neural migration and axonal and dendritic targeting during the neuronal differentiation of hiPSC-derived neurons from RTS patients²⁵. However, it will be important to replicate these results on a larger cohort of patients in order to validate the impact of CBP activity on neuronal differentiation, given the potential heterogeneity associated with hiPSC cell culture.

Among DEGS enriched in neurodevelopmental BPs, we identified 7 genes of interest encoding transcription factors and showing strong functional interaction, particularly *CA10*, *RSPO2*, *LMX1A*, *NEUROG2*, *SOX3*, and *ZIC3* (Fig. 4d). *RSPO2* encodes a member of the R-Spondin family of proteins. *RSPO2* functions in a positive feedback loop to stimulate the WNT/ β -catenin pathway. Interestingly, *RSPO2* is also involved in limb development with mutations in *RSPO2* associated with Humero-femoral hypoplasia with radiotibial ray deficiency (OMIM #618022). In agreement with changes in *RSPO2* expression, one of the most significant DEG-enriched GO terms at D10 corresponds to "positive regulation of osteoblast differentiation" with around 12% of DEGs corresponding to this BP. These data may suggest that the defect leading to the typical extremity anomalies associated with RTS phenotype may occur very early during development. This represents a future avenue to explore the skeletal phenotype of RTS patients⁴⁴.

LMX1A encodes a transcription factor that belong to the family of homeodomain and LIM-domain containing proteins. *CA10* encodes a member of the carbonic anhydrase family of zinc metalloenzymes, which catalyze the reversible hydration of carbon dioxide in various biological processes. This protein is thought to play a role in the central nervous system, especially during brain development. Both factors are involved in the central nervous system, notably in development of dopamine producing neurons during embryogenesis that is related to the WNT/ β -catenin pathway^{45,46}.

ZIC3 encodes a member of the ZIC family of C2H2-type zinc finger proteins. This nuclear protein probably functions as a transcription factor in early stages of left-right body axis formation. *ZIC3* is associated with Transcriptional regulation of pluripotent stem cells and Nervous system development and is also involved in WNT/ β -catenin pathway⁴⁷. *NEUROG2* encodes a neural-specific basic helix-loop-helix (bHLH) transcription factor that can specify a neuronal fate on ectodermal cells and is expressed in neural progenitors within the developing central and peripheral nervous systems. The *NEUROG2* gene protein product also plays a role in the differentiation and survival of midbrain dopaminergic neurons⁴⁸. *SOX3* encodes a member of the SOX (SRY-related HMG-box) family of transcription factors involved in the determination of the cell fate during embryonic development. Mutations in *SOX3* include intellectual developmental disorder, X-Linked, with panhypopituitarism (OMIM #300123). In the same way, a number of SOX proteins, including *SOX3*, antagonize the WNT/ β -catenin signaling pathway by interacting with β -catenin⁴⁹.



Multi-OMICS integration identified histone acetylation sites associated to the early transcriptional deregulation. Of the 25 CBP-dependent acetylation sites identified, 10 appear to be more specifically linked to this key step. More specifically, we identified one site for H2A (K95), four for H2B (K5, K43, K46, K108) and five for histone H3 (K18, K23, K56, K79, K122). These findings reinforce the role of CBP/p300 in the acetylation of

H2B and H3 lysine residues, while identifying novel histone marks potentially involved in the regulation of target genes during neuronal differentiation. The *NEUROG2* and *SOX3* transcription factors whose expression is decreased at D20, are strongly associated with acetylation changes at these different histone residues. We also observed a marked association between acetylation changes and *SLITKR2* (downregulated at D20 and D60) and

Fig. 4 | Biological processes (BP) related to neurodevelopment suggest altered neuronal identity in Rubinstein-Taybi syndrome (RTS). **a** Hierarchical over-representation of biological processes (BP) identified in three or more conditions based on enrichment analysis of up and downregulated DEGs at the three time points of neuronal differentiation (D10–D20–D60) in RTS patients vs controls. Data were filtered on $-1 < FC > 1$ and $FDR < 0.05$. The 50 identified Gene Ontology (GO)-terms are represented. Two branches are distinguished. The neurodevelopment related GO-terms are shown in bold and blue and their profile during neuronal differentiation is detailed in the table. We focused further analysis on the DEGS of the two most specific GO-term for each branch, brain development and neuron differentiation. **b, c** Upset plot of the two BP of interest: brain development (**b**) and neuron differentiation (**c**). As these two GOs are only identified at D20 and D60, only

the number of DEGs from these two time points are shown. Based on the profiles from the table (**a**), we identified five DEGs for “Brain development” and five DEGs for “Neuron differentiation” that are up or downregulated at D20 and upregulated at D60 (blue border). Three DEGs being common to both lists, we retained seven DEGs (**d**). **d** List of the seven selected DEGs associated to neurodevelopment. The direction of deregulation of RTS cells versus control cells is indicated for each time point according to Log FC when significant: downregulated gene in green ($\text{LogFC} < 1$) and upregulated gene in red ($\text{LogFC} > 1$). BPs associated to each gene are indicated. **e** Protein–protein interactions for the seven neurodevelopment-associated DEGs. The pink lines correspond to experimentally determined interactions, the green lines to text mining and the black lines to co-expression.

SLC18A3 (upregulated at D20), both involved in synaptic function^{50,51}. *SLITRK2* has already been identified as downregulated in other neurodevelopmental disorders, in particular X-Fragile syndrome⁵². Among well-known histone marks, Narita et al. recently showed that H3K27 acetylation is not specifically catalyzed by CBP/p300 unlike N-terminal H2Ac marks⁴⁰. Interestingly, we showed that although highly hypoacetylated throughout neuronal differentiation, H3K27ac is not associated with changes occurring at D20, suggesting a global impact on transcriptional regulation, notably of CBP/p300 targets, but not specifically linked to neuronal differentiation in RTS.

In conclusion, we provided here the first human CBP-dependent histone acetylation map during neuronal differentiation and showed the impact of CBP loss of function on the acetylation profile of H2B and H3, as previously observed in other species^{21,22,40}. Our acetylome and transcriptomic kinetic study defined a specific signature that might be associated with alteration of the neuronal identity of RTS patient’s cells. Furthermore, our data integration revealed a confidence map of RTS-specific histone acetylation marks coupled to a critical step of transcriptomic deregulation at the neural progenitor to immature neuron transition stage in RTS. More specifically, histone acetylation marks are more specifically linked to this key stage of neuronal differentiation, with a possible impact on the regulation of numerous genes linked to neurodevelopment, notably via the WNT/ β -catenin pathway. This reinforces the notion that H3K27 acetylation is not specifically catalyzed by CBP/p300. It further indicates that changes in H3K27Ac is not the main and only cause of the massive changes in gene expression observed at the transition between mature and immature neurons in RTS cells.

The definition of DNA methylation epismutations has opened a new era for accurate diagnosis and clinical assessment in a number of chromatinopathies, including RTS^{53,54}. Based on the role of CBP in shaping the epigenome and the epigenetic mechanism underlying RTS, the development of patient-derived cellular models for integration of transcriptomic data coupled together with histone acetylation profiles will likely contribute to a better definition of a specific epigenetic signature of the syndrome in order to reduce diagnostic deadlocks and open new therapeutic strategies.

Materials and methods

Samples

We enrolled four patients for which the clinical and molecular diagnosis of RTS was available. All four patients carry the *CREBBP* c.3832 C > T/p.Glu1278Lys variant. This mutation has been described to abolish the KAT activity of CBP and leads to a reduced co-activator function for CREB²⁶. All patients or guardians have provided written informed consent for the collection of samples and subsequent analysis for research purposes. The study was done in accordance with the personal protection committee (CPP Sud Est V RCB ID No.: 2019-A01637-50). All ethical regulations relevant to human research participants were followed. Primary fibroblasts were obtained from a skin upper arm biopsy. Controls are randomly chosen individuals selected in the same age range and sex representation (CT1 and CT2). Controls are neither carrier of any pathogenic genetic variant nor affected by any constitutive pathology. Fibroblasts from control patients

come from MMG U1251 biobank registered under the number dc-2018-3207. The presence of the causal mutation was verified by Sanger sequencing in the primary fibroblasts and differentiated neurons of the four RTS patients. Samples are listed and described in Table S1.

Reprogramming of fibroblasts into human Induced Pluripotent Stem Cells (hiPSC)

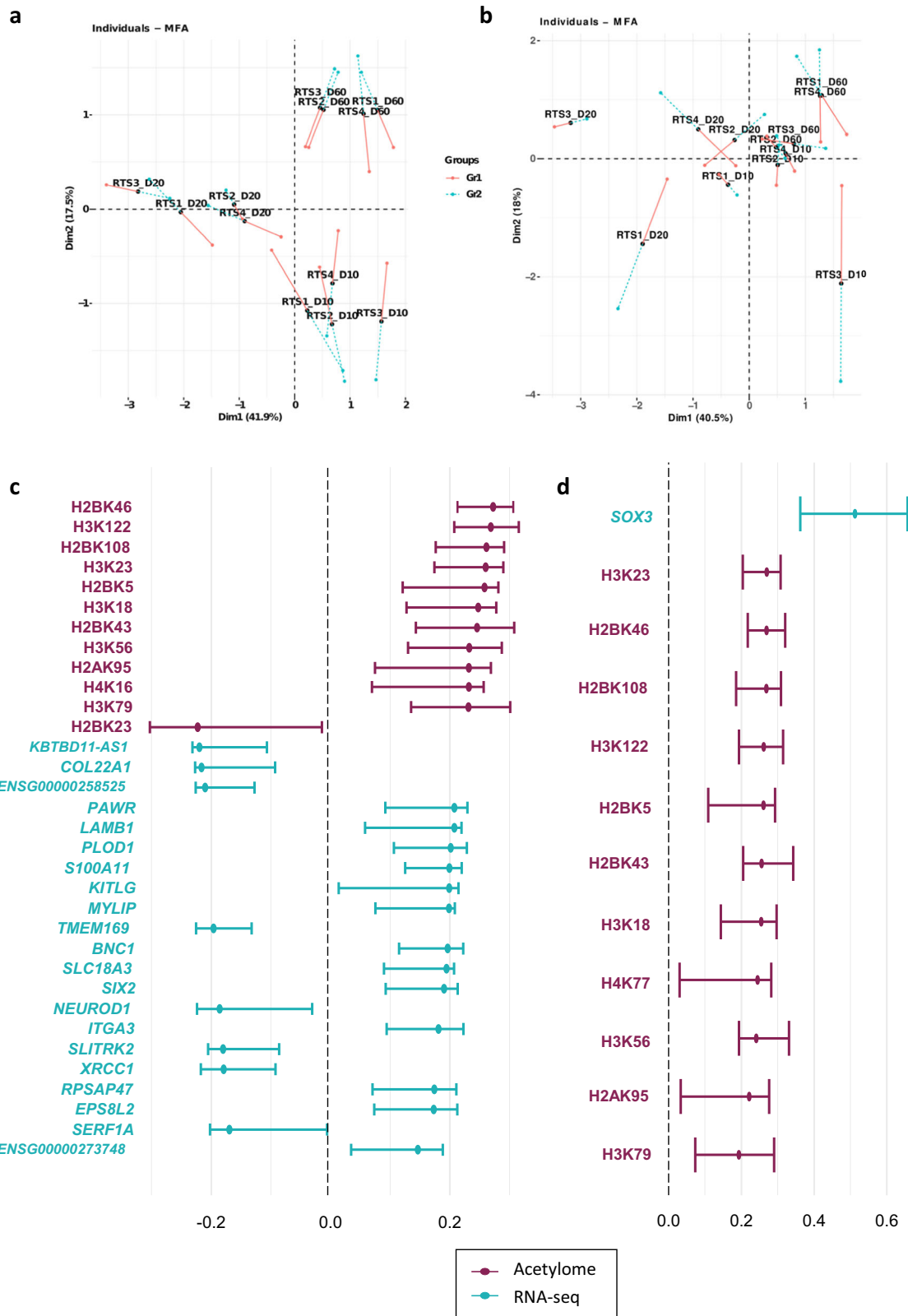
Fibroblasts from patients and healthy volunteers were reprogrammed into hiPSC at the Marseille Stem Cell (MaSC) core facility after episome electroporation. Three episomes were used, one allowing the expression of *OCT3/4* and a shRNA directed against *P53*, a second allowing the expression of *SOX2* and *KLF4* and the last allowing the expression of *L-MYC* and *LIN28*. These transcription factors, identified by Takahashi and Yamanaka³⁰, are sufficient and necessary for the reprogramming of differentiated cells into hiPSCs. For each patient, two clones were generated: RTS1L/N, RTS2I/L, RTS3A/F and RTS4B/D. Each clone was validated as described. More specifically, we verified the expression of pluripotent genes, the absence of chromosomal abnormality and the differentiation capacity by embryoid body formation⁵⁵.

Differentiation of hiPSCs into cortical and pyramidal neurons

HiPSCs were differentiated into cortical and pyramidal neurons according to a protocol adapted from Shi et al.²⁷. First, hiPSCs are cultured with Neural Induction Medium (NIM) on Matrigel-coated culture dishes. Induction towards the neuronal lineage requires the addition of a TGF β pathway inhibitor (SB431542—Sigma Aldrich, 10 μM) and a BMP pathway inhibitor (LDN193189—Sigma Aldrich, 0.2 μM) to the culture medium. The addition of NIM is considered as Day 0 (D0) for further characterizations. After the enzymatic passage of cells at D10, cells were cultured with Neural Maintenance Medium (NMM). At D17, the NMM medium was supplemented with 20 ng/ml of basic fibroblast growth factor (bFGF; PeproTech) for 4 days, allowing the expansion of neural progenitors but slowing down the differentiation into mature cortical neurons. At D20, a second enzymatic passage with dispase is performed. At D25–D30, the third enzymatic passage with accutase is performed on culture dishes treated with poly-L-Ornithine Laminin. At D60, mature cortical neurons are obtained.

Stage-specific markers

To characterize neuronal differentiation, the presence of markers specific to each stage of differentiation were analyzed: PAX6, a transcription factor and NESTIN, an intermediate filament protein is mainly produced in neuronal progenitors. Class 3 β -tubulin (or β 3-tubulin), a subunit of the microtubule specifically localized in neurons and the transcription factor TBR1, involved in cortical development were used to characterize the immature neuron stage. Microtubule-associated protein 2 (MAP2) and Neuronal Nuclei protein (NeuN) were used as markers of cortical mature neurons. The EMX1 transcription factor and metabotropic G protein-coupled glutamate receptors (mGluR5) or vGLUT1/vGLUT2, glutamate transporter associated with synaptic vesicle membranes were used as pyramidal neuron markers.



Flow cytometry

Cells were harvested by Accutase digestion and resuspended in 1× PBS + 5% FBS (Gibco). Samples are fixed and permeabilized with Cytofix/Cytoperm (BD Biosciences) for 20 min at 4 °C, and centrifuged for 5 min at 300 rpm, then 300 μL of Perm/Wash buffer (diluted in PBS 1×) is added to the pellet. The samples were centrifuged for 5 min at 300 rpm and the pellet

was resuspended in 2 × 50 μL of Perm/Wash. Each pellet was split for the anti-X (Table S2)—FITC labeling and for the REA Control (I) FITC isotype. Analysis was performed with an ACCURI C6 flow cytometer based on forward scatter (FSC-A) versus side scatter (SSC-A) for selection of live cells and removal of cell aggregates or debris. Data analysis was performed using the FlowJo software (BD Bioscience). Analysis of the fluorescent population

Fig. 5 | Integrative analysis of Acetylome and RNA-seq highlights histone marks and genes specifically involved in the crucial step of neuronal differentiation in RTS. **a** Individual plot of multifactorial analysis (MFA) integrating the two data types: Gr1 (Acetylome) data corresponds to the logFC for acetylation of 25 histones marks provided by the acetylation analysis. For data of Gr2, the logFC of the top DEG genes is provided by the DESeq2 DEG analysis. At each time points, all controls samples are pooled to serve as baseline for individual acetylation or DEG analysis of RTS samples. As in Fig. 3a, the strongest signal (component 1) separates D20 samples from D10 and D60. **b** Individual plots of MFA analysis focused on neurone development. The analysis integrates two groups data types. Gr1 are similar to in (a). For Gr2, the analysis is restricted to the logFC of the seven selected genes related to neurone development. As in panel (a), the strongest signal (component 1) for RTS samples vs controls separates D20 samples from D10 and D60. **c** The barplot shows

the Confidence Intervals for variable weights driving Component 1 of MFA analysis in (a). Only variables with robust contribution to component 1 are shown: CI do not overlap with 0 on 2000 fold Bootstrap. Except for H2BK23, all histone marks show stronger hypoacetylation for RTS samples vs controls at D20 (vs. D10 and D60). Correspondingly, positive weights shows DEGs for RTS samples vs. controls that are more strongly downregulated at D20 (vs. D10 and D60) and negative weights corresponds to DEGs for RTS vs controls that are less downregulated at D20 (vs. D10 and D60). **d** The barplot shows the Confidence Intervals for variable weights in Component 1 for the MFA in (b). Only variables with robust contribution to component 1 are shown: CI do not overlap with 0 on 500-fold Bootstrap. All variable weights are positive: for RTS samples vs. controls. SOX3 gene shows a stronger downregulation at D20 (vs. D10 and D60), as well as stronger hypoacetylation of 11 histone marks at D20 (vs. D10 and D60).

was limited to live cells. Unstained cells and control isotypes were used to determine the fluorescence background. Compensation was determined for individual fluorochromes. The gating strategy used was Forward and side scatter gating.

Immunofluorescence (IF)

Cells were washed with PBS (1×) and fixed with 4% paraformaldehyde for 20 min at RT. The slides were washed 3 times with PBS (1×). Primary antibodies (Table S2) diluted in PBS BSA 3%—Triton 0.4% were added and slides were incubated overnight at 4 °C then washed 3 times with PBS (1×). Secondary antibodies, (diluted 1/1000 in PBS BSA-3%—Triton 0.4%), were added for 1 h incubation in the dark at RT. Slides were washed with PBS (1X) and then mounted with a mounting medium (Vectashield) containing DAPI. Images were acquired using a confocal imaging system (LSM800; Zeiss). The imaging was conducted using a 20x objective lens. During the imaging process, we carefully controlled the image capture conditions to ensure consistency and reproducibility. The microscope settings, including exposure time, gain, and offset, were standardized across all samples.

Immunofluorescence quantification and analysis

PAX6, NESTIN and MAP2 staining intensity was determined as the ratio of their respective fluorescence intensity relative to the number of nuclei. An average of 10 fields were analyzed per sample. NESTIN and MAP2 morphological network was analyzed by applying an in-house deconvolution filter, adapted for neuronal analysis from Koopman et al.⁵⁶, then counting the number of objects relative to their circularity parameter. Results are given in Arbitrary Units (A.U.). $n = 2$ per controls condition and $n = 4$ per RTS patient's condition. An unpaired t test statistical analysis was performed using GraphPad. Statistical significance was determined at NS not significant, * p value < 0.05, ** p value < 0.01 and *** p value < 0.001. Error bars represent the SEM (standard error of the Mean). All data are expressed as the mean ± SEM.

RNA extraction, quality control

Total RNA was extracted using the RNeasy kit (Qiagen) following manufacturer's instructions. Quality, quantification and sizing of total RNA was evaluated using the RNA 6000 Pico assay (Agilent Technologies Ref. 5067-1513) on an Agilent 2100 Bioanalyzer system. The RNA integrity number (RIN) was calculated for each sample and only samples with RIN > 9 were kept for further use.

RT-qPCR and analysis

Reverse transcription of total RNA (1 µg) was performed using the SuperScript IV First-Strand cDNA Synthesis kit (Life Technologies) following manufacturer's instructions. Priming was performed with a mixture of oligodT and random hexamers to target all RNA. Real time qPCR assays were performed on 96 and 384 well plates on QuantStudio5 (Thermo Fisher). Primers were selected using Primer BLAST. For each amplification Sybr Green (LightCycler® 480 SYBR® Green I Master, Roche), 0.5 µM of each primer (sense and antisense) targeting each specific or housekeeper gene (Table S3) and RNase free water were added for a final volume of 8 µL.

Then 1 µL of ¼ diluted cDNA was added in each well. A technical triplicate was performed to ensure reproducibility of the results and of the proper completion of RT-qPCR steps. For each sample, the relative expression level was determined by Δ Ct quantification and normalization to the expression of the *HPRT*, and *PPIA* housekeeping genes used as standards. For analysis of the differentiation kinetics, D10 was used as the reference as most genes are not expressed in iPSCs. Statistical significance was determined using an F-test on two-way ANOVA for paired sample analysis and p -values were corrected for multiple comparison using Benjamini-Hochberg control for false discovery rate.

RNA-Seq data processing and differential expression analysis

Samples were sent to Genewiz (Azenta Life Sciences, Steiflingen, Germany) for high throughput bulk RNA sequencing according to their guidelines for sequencing on an Illumina Novaseq (2 × 150). Reads were aligned on the Human genome reference (GRCh38) using STAR (v 2.7.3). The quantification of aligned reads over the genes was also performed by STAR (GenesCounts mode). Using the resulting count matrix over all samples, the Differentially Expressed Genes (DEGs) were identified with the DESeq2 R package (v 1.26.0). DEGs with a $|\log_2\text{Foldchange}|$ cutoff ≥ 1 and a corrected p -value under 0.01 were selected for further analyses. We used the Ensembl human gene IDs identified in the DESeq2 step as input for further analyses. The raw RNA-seq data and raw count matrix were deposited at the NCBI Gene Expression Omnibus (GEO access number GSE239417).

Heatmaps were generated by the *heatmap* R package (v 1.0.12) using the normalized counts in each sample for the best DEGs. For rows and columns, the Euclidean distance measurement was used to compute the dendrograms. The color of each box in the heatmap reflects the normalized count value. In a continuous color gradient, the red values indicate overexpression, while the blue values indicate genes that are underexpressed. The expression scale was set between 6 and -4. The Volcano plots were generated using the *ggplot2* R package (v 3.4.2), with previous significance thresholds used to highlight over/underexpressed DEGs in blue while keeping all other genes in red. Venn diagrams were obtained using the *ggvenn* R package (v 0.1.10) and upset plots using the *UpSetR* R package (v 1.4.0).

Gene ontology (GO) analysis

Enrichment analyses were performed using the gProfiler2 R package (v 0.2.1). Query list was not ordered and the significance level was set to 0.05 after Benjamini-Hochberg FDR correction for multiple testing. The barplots of significant GO terms belonging to the Biological Processes (BP) were obtained using GraphPad Prism statistical package 9.5 from GraphPad Software, with the x -axis corresponding to $\log_{10}(\text{FDR})$, and GO terms on the y -axis. Percentage of DEGs associated with a given GO term is indicated on the left-colored bar plot.

Generation of DEG protein-protein interaction networks

Protein-protein interaction networks for DEGs were generated using the String software, version 11.5 (<http://www.string-db.org/>). Proteins disconnected from the network were hidden from the visualization as well as co-expression relationships.

Acetylome

- *Extraction of histones*

Total nucleosomal histones were extracted using the EpiQuik™ Total Histone Extraction Kit (EpigenTek) following manufacturer's instructions. Quality, quantification and sizing of whole histone proteins was evaluated by Western Blotting.

- *Sample preparation and protein digestion*

Protein samples were solubilized in Laemmli buffer and 5 µg of proteins were deposited onto SDS-PAGE gel 10%. After colloidal blue staining, each lane was cut out from the gel and subsequently cut in 1 mm × 1 mm gel pieces. Gel pieces were destained in 25 mM ammonium bicarbonate 50% acetonitrile (ACN), rinsed twice in ultrapure water and shrunk in ACN for 10 min. After ACN removal, gel pieces were dried at room temperature, covered with a trypsin solution (10 ng/µl in 50 mM NH₄HCO₃), rehydrated at 4 °C for 10 min, and finally incubated overnight at 37 °C. Spots were then incubated for 15 min in 50 mM NH₄HCO₃ at room temperature with rotary shaking. The supernatant was collected, and an H₂O/ACN/HCOOH (47.5:47.5:5) extraction solution was added onto gel slices for 15 min. The extraction step was repeated twice. Supernatants were pooled and dried in a vacuum centrifuge. Digests were finally solubilized in 0.1% HCOOH.

- *nLC-MS/MS analysis and Label-Free Quantitative Data Analysis*

The peptide mixture was analyzed on an Ultimate 3000 nanoLC system (Dionex, Amsterdam, The Netherlands) coupled to an Electrospray Orbitrap Fusion™ Lumos™ Tribrid™ Mass Spectrometer (Thermo Fisher Scientific, San Jose, CA). Ten microliters of peptide digests were loaded onto a 300-µm-inner diameter × 5-mm C₁₈ PepMap™ trap column (LC Packings) at a flow rate of 10 µL/min. The peptides were eluted from the trap column onto an analytical 75-mm id × 50-cm C18 Pep-Map column (LC Packings) with a 4–30% linear gradient of solvent B in 71 min (solvent A was 0.1% formic acid and solvent B was 0.1% formic acid in 80% ACN) followed by a 30–90% gradient of solvent B in 15 min. The separation flow rate was set at 300 nL/min. The mass spectrometer operated in positive ion mode at a 1.9-kV needle voltage. Data were acquired using the Xcalibur 4.4 software in a data-dependent mode. MS scans (*m/z* 375–1500) were recorded in the Orbitrap at a resolution of $R = 120,000$ (@ *m/z* 200) and an AGC target of 4×10^5 ions collected within 50 ms. Dynamic exclusion was set to 30 s and top speed fragmentation in HCD mode was performed over a 3 s cycle. MS/MS scans were collected in the Orbitrap with a resolution of 30,000 and maximum fill time of 54 ms. Only +2 to +7 charged ions were selected for fragmentation. Other settings were as follows: no sheath nor auxiliary gas flow, heated capillary temperature, 275 °C; normalized HCD collision energy of 28%, isolation width of 1.6 *m/z*, AGC target of 5×10^4 and normalized AGC target of 100%. Monoisotopic precursor selection (MIPS) was set to Peptide and an intensity threshold was set to 2.5×10^4 .

- *Database search and results processing*

Data were searched by SEQUEST through Proteome Discoverer 2.5 (Thermo Fisher Scientific Inc.) against a Swissprot human database (20,324 entries in v2021-06-03). Spectra from peptides higher than 5000 Da or lower than 350 Da were rejected. Precursor Detector node was included. Search parameters were as follows: mass accuracy of the monoisotopic peptide precursor and peptide fragments was set to 10 ppm and 0.02 Da respectively. Only b- and y-ions were considered for mass calculation. Three search algorithm were used simultaneously: In Sequest HT, oxidation of Methionines (+16 Da), phosphorylation of Serine and Threonine (+80 Da), Acetylation (+42 Da), Methylation (+14 Da), Dimethylation (+28 Da) and Trimethylation (+42 Da) of lysines, Methionine loss (−131 Da), Methionine loss with acetylation (−89 Da) and protein N-terminal acetylation (+42 Da) were considered as variable modifications while

carbamidomethylation of Cysteines (+57 Da) was considered as a fixed modification. Four missed trypsin cleavages were allowed. Amanda and Byonic were only used for searching a smaller database consisting of 89 proteins database consisting of a preliminary search. Amanda considered oxidation of Methionines (+16 Da), acetylation (+42 Da) and methylation (+14 Da) as variable modification while Byonic included in addition di- and tri-methylation of Lysines. Peptide validation was performed using Percolator algorithm⁵⁷ or Target Decoy PSM Validator (for Byonic) and only “high confidence” peptides were retained corresponding to a 1% False Positive Rate at peptide level. Peaks were detected and integrated using the Minora algorithm embedded in Proteome Discoverer. Normalization was performed based on the total human protein amount. Protein ratios were calculated as the median of all possible pairwise peptide ratios. A *t*-test was calculated based on background population of peptides or proteins. Quantitative data were considered for proteins quantified by a minimum of two peptides and a statistical *p*-value lower than 0.05.

- *Bioinformatic analysis*

The proteins and peptides predicted in the previous step were filtered in order to keep only the proteins coding for the histones. For these proteins we keep only the peptides having at least one modification of the acetylation type. All isoforms are conserved for the analysis, the peptides can therefore present different acetylation for the same protein. A normalization was next performed based on the master protein quantification in these samples. Since several predicted proteins can encode the same histone, it is essential to make the acetylation positions comparable. For this we have produced a multiple alignment of the protein coding for each histone and translated the positions in a common referential. For each comparison and for each histone acetylated position the acetylation ratio was calculated as the median of all possible pairwise ratios for each concerned sample and peptide (non-nested ratio calculation with pairwise ratio approach). A position was considered differentially acetylated for $|\log_2 \text{acRatio}| \geq 1$.

Multi factorial analysis

To produce a joint analysis of Histone acetylation marks and Gene Expression, a Multi Factorial Analysis (MFA) framework introduced in Escoffier and Pages was performed³¹. In our case, we have a limited number of samples and a common approach is to reduce the dimension of the data. By doing so using MFA, we can find associations across the two omics datasets. To better homogenize the two datasets, we used Log Fold change (logFC) for (i) acetylation values and (ii) gene expression levels between RTS vs. controls samples, grouped by time and patient, resulting in 12 samples for each dataset. The first MFA components were obtained using the *FactomineR*⁵⁸ and *factoextra* packages. The bootstrap framework available in the *RGCCA* package⁵⁹ was then used to calculate 2000 permutations of the first component of the MFA analysis to compute the confidence interval (CI) for the loading of variables from the different groups studied. The CI barplots were obtained using the *RGCCA* package. In these barplots, variables for which the CI does not extend over the 0 value can be safely associated with the component.

Reporting summary

Further information on research design is available in the Nature Portfolio Reporting Summary linked to this article.

Data availability

The raw RNA-seq data and raw count matrix were deposited at the NCBI Gene Expression Omnibus (GEO access number GSE239417). The numerical source data for all graphs in the manuscript can be found in Supplementary Data 1 file.

Received: 29 August 2023; Accepted: 23 September 2024;

Published online: 15 October 2024

References

- Fahrner, J. A. & Bjornsson, H. T. Mendelian disorders of the epigenetic machinery: postnatal malleability and therapeutic prospects. *Hum. Mol. Genet.* **28**, R254–R264 (2019).
- Rubinstein, J. H. Broad thumb-hallux (Rubinstein-Taybi) syndrome 1957–1988. *Am. J. Med. Genet.* **37**, 3–16 (1990).
- Hennekam, R. C. M. Rubinstein-Taybi syndrome. *Eur. J. Hum. Genet.* **14**, 981–985 (2006).
- Van Gils, J., Magdinier, F., Fergelot, P. & Lacombe, D. Rubinstein-Taybi syndrome: a model of epigenetic disorder. *Genes* **12**, 968 (2021).
- Bartsch, O. et al. DNA sequencing of CREBBP demonstrates mutations in 56% of patients with Rubinstein-Taybi syndrome (RSTS) and in another patient with incomplete RSTS. *Hum. Genet.* **117**, 485–493 (2005).
- Fergelot, Patricia et al. Phenotype and genotype in 52 patients with Rubinstein-Taybi syndrome caused by EP300 mutations. *Am. J. Med. Genet. A.* **170**, 3069–3082 (2016).
- Giles, R. H., Dauwse, H. G., van Ommen, G. J. & Breuning, M. H. Do human chromosomal bands 16p13 and 22q11-13 share ancestral origins? *Am. J. Hum. Genet.* **63**, 1240–1242 (1998).
- Bartholdi, D. et al. Genetic heterogeneity in Rubinstein-Taybi syndrome: delineation of the phenotype of the first patients carrying mutations in EP3. *J. Med. Genet.* **44**, 327–333 (2007).
- Allis, C. D. et al. New nomenclature for chromatin-modifying enzymes. *Cell* **131**, 633–636 (2007).
- Bedford, D. C., Kasper, L. H., Fukuyama, T. & Brindle, P. K. Target gene context influences the transcriptional requirement for the KAT3 family of CBP and p300 histone acetyltransferases. *Epigenetics* **5**, 9–15 (2010).
- Wang, L., Tang, Y., Cole, P. A. & Marmorstein, R. Structure and chemistry of the p300/CBP and Rtt109 histone acetyltransferases: implications for histone acetyltransferase evolution and function. *Curr. Opin. Struct. Biol.* **18**, 741–747 (2008).
- Boija, A. et al. CBP regulates recruitment and release of promoter-proximal RNA polymerase II. *Mol. Cell* **68**, 491–503.e5 (2017).
- Dancy, B. M. & Cole, P. A. Protein Lysine Acetylation by p300/CBP. *Chem. Rev.* **115**, 2419–2452 (2015).
- Goodman, R. H. & Smolik, S. CBP/p300 in cell growth, transformation, and development. *Genes Dev.* **14**, 1553–1577 (2000).
- Oike, Y. et al. Truncated CBP protein leads to classical Rubinstein-Taybi Syndrome phenotypes in mice: implications for a dominant-negative mechanism. *Hum. Mol. Genet.* **8**, 387–396 (1999).
- Viosca, J., Lopez-Atalaya, J. P., Olivares, R., Eckner, R. & Barco, A. Syndromic features and mild cognitive impairment in mice with genetic reduction on p300 activity: Differential contribution of p300 and CBP to Rubinstein-Taybi syndrome etiology. *Neurobiol. Dis.* **37**, 186–194 (2010).
- Monsey, M. S., Ota, K. T., Akingbade, I. F., Hong, E. S. & Schafe, G. E. Epigenetic alterations are critical for fear memory consolidation and synaptic plasticity in the lateral amygdala. *PLoS ONE* **6**, e19958 (2011).
- Bousiges, O. et al. Spatial memory consolidation is associated with induction of several lysine-acetyltransferase (histone acetyltransferase) expression levels and H2B/H4 acetylation-dependent transcriptional events in the rat hippocampus. *Neuropsychopharmacology* **35**, 2521–2537 (2010).
- Lubin, F. D. & Sweatt, J. D. T. H. E. IκB kinase regulates chromatin structure during reconsolidation of conditioned fear memories. *Neuron* **55**, 942–957 (2007).
- Bredy, T. W. et al. Histone modifications around individual BDNF gene promoters in prefrontal cortex are associated with extinction of conditioned fear. *Learn. Mem.* **14**, 268–276 (2007).
- Lopez-Atalaya, J. P. et al. Histone acetylation deficits in lymphoblastoid cell lines from patients with Rubinstein-Taybi syndrome. *J. Med. Genet.* **49**, 66–74 (2012).
- Weinert, B. T. et al. Time-resolved analysis reveals rapid dynamics and broad scope of the CBP/p300 Acetylome. *Cell* **174**, 231–244.e12 (2018).
- Cembrowski, M. S. & Spruston, N. Heterogeneity within classical cell types is the rule: lessons from hippocampal pyramidal neurons. *Nat. Rev. Neurosci.* **20**, 193–204 (2019).
- Alari, V. et al. iPSC-derived neurons of CREBBP- and EP300-mutated Rubinstein-Taybi syndrome patients show morphological alterations and hypoexcitability. *Stem Cell Res.* **30**, 130–140 (2018).
- Calzari, L. et al. Transcriptome analysis of iPSC-derived neurons from Rubinstein-Taybi patients reveals deficits in neuronal differentiation. *Mol. Neurobiol.* **57**, 3685–3701 (2020).
- Kalkhoven, E. et al. Loss of CBP acetyltransferase activity by PHD finger mutations in Rubinstein-Taybi syndrome. *Hum. Mol. Genet.* **12**, 441–450 (2003).
- Shi, Y., Kirwan, P. & Livesey, F. J. Directed differentiation of human pluripotent stem cells to cerebral cortex neurons and neural networks. *Nat. Protoc.* **7**, 1836–1846 (2012).
- Zucconi, B. E. et al. Modulation of p300/CBP acetylation of nucleosomes by bromodomain ligand I-CBP112. *Biochemistry* **55**, 3727–3734 (2016).
- Escofier, B. & Pagès, J. *Analyses Factorielles Simples et Multiples. Objectifs Méthodes et Interprétation.* 328 p. (Dunod, 2008).
- Takahashi, K. & Yamanaka, S. Induction of pluripotent stem cells from mouse embryonic and adult fibroblast cultures by defined factors. *Cell* **126**, 663–676 (2006).
- Zeng, X. et al. Concise review: modeling central nervous system diseases using induced pluripotent stem cells. *Stem Cells Transl. Med.* **3**, 1418–1428 (2014).
- Boissart, C. et al. Differentiation from human pluripotent stem cells of cortical neurons of the superficial layers amenable to psychiatric disease modeling and high-throughput drug screening. *Transl. Psychiatry* **3**, e294 (2013).
- Hrvoj-Mihic, B., Marchetto, M. C. N., Gage, F. H., Semendeferi, K. & Muotri, A. R. Novel tools, classic techniques: evolutionary studies using primate pluripotent stem cells. *Biol. Psychiatry* **75**, 929–935 (2014).
- Espuny-Camacho, I. et al. Pyramidal neurons derived from human pluripotent stem cells integrate efficiently into mouse brain circuits in vivo. *Neuron* **77**, 440–456 (2013).
- Song, S., Song, S., Zhang, H., Cuevas, J. & Sanchez-Ramos, J. Comparison of neuron-like cells derived from bone marrow stem cells to those differentiated from adult brain neural stem cells. *Stem Cells Dev.* **16**, 747–756 (2007).
- Lipinski, M. et al. KAT3-dependent acetylation of cell type-specific genes maintains neuronal identity in the adult mouse brain. *Nat. Commun.* **11**, 2588 (2020).
- Gupta, A. et al. The mammalian ortholog of Drosophila MOF that acetylates histone H4 lysine 16 is essential for embryogenesis and oncogenesis. *Mol. Cell. Biol.* **28**, 397–409 (2008).
- Huang, F. et al. Histone acetyltransferase Enok regulates oocyte polarization by promoting expression of the actin nucleation factor spire. *Genes Dev.* **28**, 2750–2763 (2014).
- Chen, L.-T., Luo, M., Wang, Y.-Y. & Wu, K. Involvement of Arabidopsis histone deacetylase HDA6 in ABA and salt stress response. *J. Exp. Bot.* **61**, 3345–3353 (2010).
- Narita, T. et al. Acetylation of histone H2B marks active enhancers and predicts CBP/p300 target genes. *Nat. Genet.* **55**, 679–692 (2023).
- Chen, H. et al. MacroH2A1.1 and PARP-1 cooperate to regulate transcription by promoting CBP-mediated H2B acetylation. *Nat. Struct. Mol. Biol.* **21**, 981–989 (2014).
- Das, C., Lucia, M. S., Hansen, K. C. & Tyler, J. K. CBP/p300-mediated acetylation of histone H3 on lysine 56. *Nature* **459**, 113–117 (2009).
- Tropberger, P. et al. Regulation of transcription through acetylation of H3K122 on the lateral surface of the histone octamer. *Cell* **152**, 859–872 (2013).

44. Babu, A. et al. Chemical and genetic rescue of an ep300 knockdown model for Rubinstein Taybi Syndrome in zebrafish. *Biochim. Biophys. Acta* **1864**, 1203–1215 (2018).
45. Kazanskaya, O. et al. R-Spondin2 is a secreted activator of Wnt/beta-catenin signaling and is required for Xenopus myogenesis. *Dev. Cell* **7**, 525–534 (2004).
46. Hoekstra, E. J. et al. Lmx1a encodes a rostral set of mesodiencephalic dopaminergic neurons marked by the Wnt/B-catenin signaling activator R-spondin 2. *PLoS ONE* **8**, e74049 (2013).
47. Winata, C. L. et al. Genome wide analysis reveals Zic3 interaction with distal regulatory elements of stage specific developmental genes in zebrafish. *PLoS Genet* **9**, e1003852 (2013).
48. Lin, H.-C. et al. NGN2 induces diverse neuron types from human pluripotency. *Stem Cell Rep.* **16**, 2118–2127 (2021).
49. Bernard, P. & Harley, V. R. Acquisition of SOX transcription factor specificity through protein-protein interaction, modulation of Wnt signalling and post-translational modification. *Int. J. Biochem. Cell Biol.* **42**, 400–410 (2010).
50. Beaubien, F., Raja, R., Kennedy, T. E., Fournier, A. E. & Cloutier, J.-F. Slitrk1 is localized to excitatory synapses and promotes their development. *Sci. Rep.* **6**, 27343 (2016).
51. Varoqui, H. & Erickson, J. D. Active transport of acetylcholine by the human vesicular acetylcholine transporter. *J. Biol. Chem.* **271**, 27229–27232 (1996).
52. Boland, M. J. et al. Molecular analyses of neurogenic defects in a human pluripotent stem cell model of fragile X syndrome. *Brain. J. Neurol.* **140**, 582–598 (2017).
53. Aref-Eshghi, E. et al. Evaluation of DNA methylation epigenatures for diagnosis and phenotype correlations in 42 Mendelian neurodevelopmental disorders. *Am. J. Hum. Genet.* **106**, 356–370 (2020).
54. Kerkhof, J. et al. DNA methylation epigenature testing improves molecular diagnosis of Mendelian chromatinopathies. *Genet. Med.* **24**, 51–60 (2022).
55. Martí, M. et al. Characterization of pluripotent stem cells. *Nat. Protoc.* **8**, 223–253 (2013).
56. Koopman, W. J. H. et al. Mitochondrial network complexity and pathological decrease in complex I activity are tightly correlated in isolated human complex I deficiency. *Am. J. Physiol. Cell Physiol.* **289**, C881–C890 (2005).
57. Käll, L., Canterbury, J. D., Weston, J., Noble, W. S. & MacCoss, M. J. Semi-supervised learning for peptide identification from shotgun proteomics datasets. *Nat. Methods* **4**, 923–925 (2007).
58. Lê, S., Josse, J. & Husson, F. FactoMineR: an R Package for Multivariate Analysis. *J. Stat. Softw.* **25**, 1–18 (2008).
59. Tenenhaus, M., Tenenhaus, A. & Groenen, P. J. F. Regularized generalized canonical correlation analysis: a framework for sequential multiblock component methods. *Psychometrika* <https://doi.org/10.1007/s11336-017-9573-x> (2017).

Acknowledgements

We are indebted and thank the French support group (www.afsrt.com) and all patients for participating in this study. We acknowledge the *Centre de Ressources Biologiques Plurithématique, Bordeaux Biothèque Santé*. Funding This study was funded by the Rubinsten–Taybi Syndrome Foundation, the University Hospital of Bordeaux and *Agence de la Biomédecine*. The project leading to this publication has received funding from the Excellence Initiative of Aix-Marseille University–A*Midex, a French “investissement d’avenir program” AMX-19-IET-007 through the Marseille Maladies Rares (MarMaRa) Institute and funding to J.V.G. J.P.T.

was funded by Agence Nationale de la Recherche, ANR-18-CE15-0014-03, Epipro Project.

Author contributions

J.V.G. conceptualized and designed the study in collaboration with P.F., contributed to the experimental design, performed the experiments, analyzed data, obtained funding and wrote the paper, with the contribution of P.F. and F.M. S.K. performed the multi-Omics analysis and contributed to all bioinformatic analysis. A.B. performed transcriptomic data analysis with the contribution of S.N. and R.C. and acetylation data analysis with the contribution of S.C. S.L.N. contributed to images analysis. S.N., under the supervision of J.V.G., and performed RTq-PCR analysis. S.C. and C.T. contributed to the conceptual and experimental strategy for acetylation and performed mass spectrometry. J.P.T. was involved in the conceptual design and characterization of hiPSC-derived neurons from RTS patients and controls with the contribution of N.B. C.E.Y. and N.B. performed the reprogramming of hiPSC from fibroblasts of SRT patients and provided controls. D.L. diagnosed RTS patients and performed skin biopsies, with the contribution of J.V.G. and P.F. F.M. supervised all experiments and the writing of the paper.

Competing interests

The authors declare no competing interest.

Additional information

Supplementary information The online version contains supplementary material available at <https://doi.org/10.1038/s42003-024-06939-3>.

Correspondence and requests for materials should be addressed to Julien Van Gils.

Peer review information *Communications Biology* thanks the anonymous reviewers for their contribution to the peer review of this work. Primary Handling Editors: Edwina McGlinn and Joao Valente.

Reprints and permissions information is available at <http://www.nature.com/reprints>

Publisher’s note Springer Nature remains neutral with regard to jurisdictional claims in published maps and institutional affiliations.

Open Access This article is licensed under a Creative Commons Attribution-NonCommercial-NoDerivatives 4.0 International License, which permits any non-commercial use, sharing, distribution and reproduction in any medium or format, as long as you give appropriate credit to the original author(s) and the source, provide a link to the Creative Commons licence, and indicate if you modified the licensed material. You do not have permission under this licence to share adapted material derived from this article or parts of it. The images or other third party material in this article are included in the article’s Creative Commons licence, unless indicated otherwise in a credit line to the material. If material is not included in the article’s Creative Commons licence and your intended use is not permitted by statutory regulation or exceeds the permitted use, you will need to obtain permission directly from the copyright holder. To view a copy of this licence, visit <http://creativecommons.org/licenses/by-nc-nd/4.0/>.

© The Author(s) 2024